Two-body dissociation of formic acid following double ionization by ultrafast laser pulses

T. Severt,[1] Darwin R. Daugaard [●],[2,3] Tiana Townsend,[2] F. Ziaee,[1] K. Borne,[1] S. Bhattacharyya [●],[1] K. D. Carnes [●],[1]
D. Rolles,[1] A. Rudenko,[1] E. Wells [●],[2,*] and I. Ben-Itzhak [●][1,†]

[1]*J. R. Macdonald Laboratory, Physics Department, Kansas State University, Manhattan, Kansas 66506, USA*
[2]*Department of Physics, Augustana University, Sioux Falls, South Dakota 57197, USA*
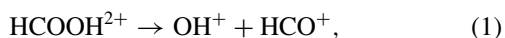[3]*Dell Rapids High School, Dell Rapids, South Dakota 57022, USA*

We studied the fragmentation of planar formic acid (HCOOH) molecules following their double ionization by intense ultrashort laser pulses. Deuterium tagging (i.e., HCOOD) combined with coincidence momentum imaging measurements of all fragment ions enabled determination of the role of the hydroxyl and carboxyl hydrogen atoms in the breakup. Specifically, we observe a strong preference for the hydroxyl (OD) group to remain intact in a $HCOOD^{2+} \rightarrow OD^+ + HCO^+$ fragmentation, which is an order of magnitude more likely than $OH^+ + DCO^+$. An even larger preference for breaking the H-C bond over the O-H bond is observed in the $H^+ + DCO_2^+$ and $D^+ + HCO_2^+$ deprotonation channels. Bond rearrangement, leading to H_2^+ or H_2O^+ formation, exhibits no isotopic preference. The kinetic-energy-release distributions of the $OH^+ + DCO^+$ and $O^+ + H_2CO^+$ breakup channels suggest that more than one process contributes to these final products, although further theoretical work is needed to identify the specific paths.

I. INTRODUCTION

Studies of complex dynamics in polyatomic molecules initiated by intense laser pulses continue to be an active area of research both due to fundamental interest and as a step toward improving control of chemical processes. Roaming of a neutral H_2 moiety [1–6], hydrogen migration [7–24], and bond rearrangement [5,6,25–40], which involves the breaking and subsequent formation of chemical bonds between different atoms, are some of the processes that have come under scrutiny in recent years.

Within this context, the fragmentation of formic acid, HCOOH, is interesting since it is a relatively complex molecule despite having only five atoms. The two hydrogen atoms are not equivalent, as one is on a carboxyl site and the other is on a hydroxyl site, and the molecule, while planar, has no further symmetries. Tunneling between local minima on both the neutral [41] and monocation [42] potential-energy surfaces induces changes in molecular geometry. HCOOH is achiral in the ground state, but an approximately 6 eV vertical transition causes pyramidalization and formation of a chiral configuration [43,44], which has been used as a basis for studying enantioselective fragmentation [45]. Due to these features, HCOOH has rich structural dynamics that have been the subject of a number of previous studies [41,42,45–47].
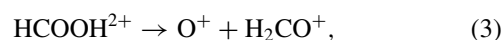
The possible two-body dissociation channels of the formic acid dication can be categorized into channels that could occur via a simple bond cleavage, such as hydroxyl formation,
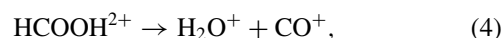
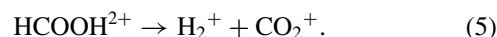$$HCOOH^{2+} \rightarrow OH^+ + HCO^+, \qquad (1)$$

deprotonation,

$$HCOOH^{2+} \rightarrow H^+ + HCO_2^+, \qquad (2)$$

and deoxygenation,

$$HCOOH^{2+} \rightarrow O^+ + H_2CO^+, \qquad (3)$$

or dissociation that involves hydrogen migration and bond rearrangement, such as water formation,

$$HCOOH^{2+} \rightarrow H_2O^+ + CO^+, \qquad (4)$$

and hydrogen formation,

$$HCOOH^{2+} \rightarrow H_2^+ + CO_2^+. \qquad (5)$$

The latter two processes are interesting because of the complex behavior needed to form the new molecular ions. We note that the first three processes could also occur through more complex dynamics than a single bond cleavage. For example, hydroxyl formation [Eq. (1)] could include the migration of hydrogen atoms rather than simple bond cleavage, but these differences are difficult to detect when the hydrogen atoms are identical.

In previous work, Wang and coworkers examined dissociation of $HCOOH^{2+}$ following double ionization by an intense laser pulse [46,47]. Their calculations showed that the lowest singlet and triplet states of $HCOOH^{2+}$ have different geometries. In the singlet state, the molecular ion is nearly linear, with OH groups on each side of the central carbon atom. This configuration is not stable and commonly leads to $HOCOH^{2+} \rightarrow OH^+ + HCO^+$, where the lifetime of $HCOOH^{2+}$ was estimated to be around 150 fs [47]. According to Wang *et al.*, further bond-rearrangement processes, which often include hydrogen migration, are less likely to proceed from the singlet ground state due to the initial separation

---
*eric.wells@augie.edu
†ibi@phys.ksu.edu

of the hydrogen atoms. On the other hand, they argue that the triplet ground state of the dication closely resembles the neutral geometry and thus more easily facilitates hydrogen migration.

In this article, we extend the studies of Wang *et al.* [46,47] by measuring the branching ratio for two-body dissociation following double ionization of both HCOOH and HCOOD targets. The advantage of deuterium tagging is that it distinguishes the hydroxyl hydrogen from the carboxyl hydrogen. Specifically, in HCOOD, the hydrogen atom (the "carboxyl hydrogen") is attached, via the carbon atom, to the carboxyl group that comprises the rest of the molecule. The carboxyl group itself contains the deuterium atom that is bound to the oxygen in the hydroxyl group ("the hydroxyl hydrogen"). In the hydroxyl formation [Eq. (1)] and deprotonation [Eq. (2)] processes, the presence of the deuterium atom in the hydroxyl group distinguishes situations in which the hydroxyl group remains intact from those in which the O and D separate.

Both hydroxyl formation and deprotonation show significantly different kinetic energy release (KER) and angular dependence (discussed in the Appendix) depending on the final-state configuration of the hydrogen atoms. In the water [Eq. (4)] and hydrogen [Eq. (5)] formation channels involving bond rearrangement, deuterium tagging allows the study of isotopic effects. Under the conditions in this study we observe no significant difference in the isotopologue-specific branching ratios and angular distributions of hydrogen and water formation.

II. EXPERIMENTAL METHOD

In the present measurements, the laser pulses were produced by a Ti:sapphire laser located in the J. R. Macdonald Laboratory known as PULSAR [48]. PULSAR produces pulses with 25-fs (FWHM in intensity) pulse duration, a central wavelength of 780 nm, and a maximum pulse energy of 2 mJ at a repetition rate of 10 kHz. The linearly polarized pulses were focused, by an $f = 7.5$ cm spherical mirror to a peak intensity of 2×10^{15} W/cm^2, onto randomly oriented target molecules in the supersonic molecular beam of the apparatus. The laser polarization is pointed along the time-of-flight axis of the spectrometer. The base pressure in the spectrometer region was below 2×10^{-10} Torr. Both HCOOH and HCOOD gas targets were measured separately, as described in the following section.

We employed cold-target recoil-ion momentum spectroscopy (COLTRIMS) [49–51] and measured all ionic fragment momenta on a molecule-by-molecule basis, enabling identification of dissociation channels. In this experiment, electrons were not detected. The data analysis procedure was very similar to the one described by Zhao *et al.* [38]. Briefly, each two-body double-ionization channel was identified on a coincidence-time-of-flight map. The laser-molecule interaction point, target gas jet velocity, and spectrometer parameters are calibrated by considering all coincidence channels simultaneously and by using the expected symmetries about the laser polarization axis [38]. Following conversion of the measured position and time of each hit on the detector to momentum space in the laser frame of reference, momentum conservation is used to separate true two-body
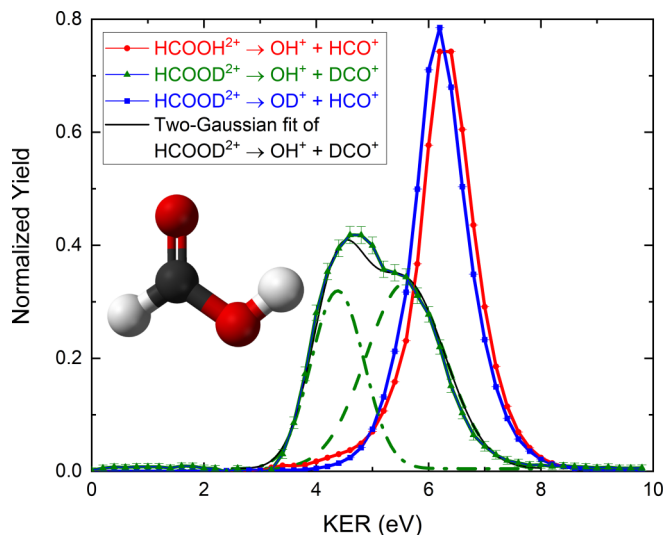

FIG. 1. Normalized yield of the hydroxyl formation channels [Eqs. (1), (6), and (7)] as a function of KER. For easier comparison of the features of the KER distribution, the yield of each channel is normalized so that the integral of each KER distribution is 1. The bond-rearrangement channel (7) is also fit with a two-Gaussian curve, indicated by the thin black line. The individual curves that contribute to the fit are shown by the dashed and dash-dotted olive lines. The inset shows a ball-and-stick model of the ground *trans* vibrational state of neutral HCOOH.

dissociation channels from the background. In some channels, contributions that arise from two different parent molecules being ionized in the same pulse, i.e., false coincidences, pass through the momentum-conservation conditions. To mimic such contributions, we randomly pair hits from different laser shots to reproduce the distribution of false coincidences. Following normalization to a channel that can arise only from a false coincidence, we subtract the artificially generated false-coincidence momentum distribution from the measured momentum distribution. [38,52]. Finally, the symmetry about the laser polarization axis is used to correct for anisotropies in the position-dependent detection efficiency.

While the formic acid is introduced at room temperature, the expansion of the molecular beam through the nozzle into vacuum leads to internal cooling of the molecules [49–51]. Thus, room temperature establishes an upper limit on the vibrational temperature of the formic-acid target, and our best estimate of the rotational target temperature is around 100 K. This means that the ground vibrational state of the *trans* configuration, illustrated in the inset in Fig. 1, is the only vibrational state with a meaningful population [53,54]. Since the rotational target temperature is much higher than the characteristic rotational temperatures [55] of formic acid, many rotational states can initially be populated.

The choice of laser intensity used in the experiment was motivated by a desire to concurrently examine ionization creating HCOOH^{3+} and even higher charge states (which will be discussed in future work). Thus, there are many dissociation channels with higher charge states observed in the data. In the present analysis, which examines double ionization followed by two-body breakup of the molecule, the
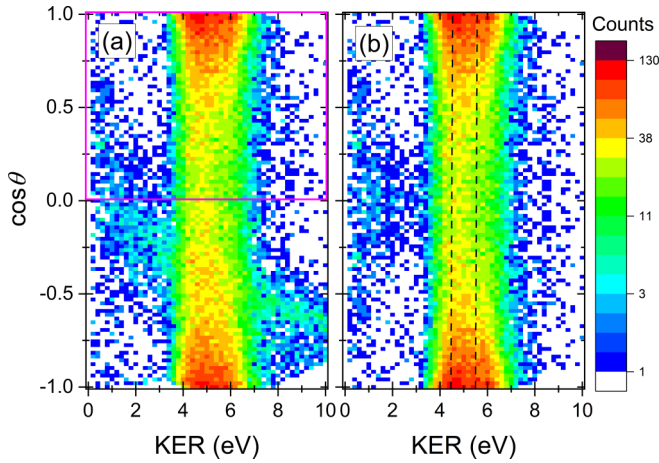
FIG. 2. The number of $HCOOD^{2+} \rightarrow OH^+ + DCO^+$ events (log scale) as a function of KER and $\cos\theta$, where θ is the angle between the OH^+ fragment and the laser polarization. (a) The spectra after momentum-conservation requirements and random-coincidence subtraction, which still leaves contamination from another channel running diagonally through the lower half of the panel. (b) The same plot for the two-body channel after mirroring the $\cos\theta > 0$ data within the magenta rectangle onto the $\cos\theta < 0$ region of the plot. The two dashed lines at 4.4 and 5.6 eV mark the locations of the KER peaks of the two-Gaussian fit shown in Fig. 1.

contributions of the associated dissociation channels with higher charge states sometimes are not entirely separated from the two-body channels using the methods described in the previous paragraph. An example is shown in Fig. 2 for the $HCOOD^{2+} \rightarrow OH^+ + DCO^+$ dissociation channel. In that plot, the two-body channel, which forms the vertical stripe around 4–6 eV, is intersected by events that curve from the middle left to bottom right in Fig. 2(a). The curvature arises because the contamination channel contains a fragment with a different mass (e.g., O^+ instead of OH^+) than the channel of interest and therefore the momentum of the contamination channel is calculated incorrectly. While subtracting this contribution is possible for many three-body contaminations such as $H^+ + O^+ + DCO^+$, we used a simpler strategy in this work. Specifically, a selection of data can be used to reconstruct, via reflection of the data about $\cos\theta = 0$, the two-body channel without the background. The estimated systematic uncertainty introduced by this procedure is included in the branching-ratio results.

III. RESULTS AND DISCUSSION

When the HCOOD isotopologue is used as a target, hydroxyl formation [Eq. (1)] separates into two distinguishable products,

$$HCOOD^{2+} \rightarrow OD^+ + HCO^+ \qquad (6)$$

$$\rightarrow OH^+ + DCO^+, \qquad (7)$$
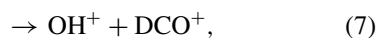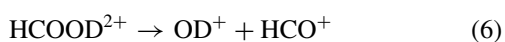
where OD^+ forms with the hydroxyl deuterium, while OH^+ formation involves the carboxyl hydrogen, indicating hydrogen migration to the lone oxygen or scrambling of the H and D. Likewise, deprotonation [Eq. (2)] separates into two channels that produce either a proton from the carboxyl site

or a deuteron from the hydroxyl site,

$$HCOOD^{2+} \rightarrow H^+ + DCO_2^+ \qquad (8)$$

$$\rightarrow D^+ + HCO_2^+. \qquad (9)$$
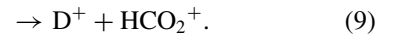
All the other dissociation channels of HCOOD (deoxygenation, water formation, and hydrogen formation) contain both hydrogen and deuterium atoms on the same fragment,

$$HCOOD^{2+} \rightarrow O^+ + HDCO^+ \qquad (10)$$

$$\rightarrow HDO^+ + CO^+ \qquad (11)$$

$$\rightarrow HD^+ + CO_2^+. \qquad (12)$$
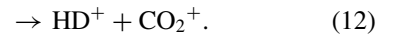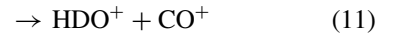
Thus, Eqs. (10)–(12) may result in isotopic differences from the analogous HCOOH cases but will not yield site specificity as it does for the hydroxyl formation or deprotonation channels. The deuterated water [Eq. (11)] and hydrogen formation [Eq. (12)] channels offer an opportunity to see whether the mass difference influences the bond-rearrangement processes.

The measured two-body branching ratios from double ionization are shown in Table I. The branching ratio is defined as the yield of the listed dissociation channel divided by the sum of all the observed two-body dissociation channels associated with double ionization from that specific isotopologue. Possible two-body dissociation channels (e.g., $C^+ + H_2O_2^+$) that are not listed in Table I were not observed in this experiment.

A. Hydroxyl formation

Hydroxyl formation is the most likely two-body dissociative double-ionization process. Deuterium tagging further characterizes this process, indicating that formation of a hydroxyl ion by simple bond cleavage [Eq. (6)] is the most common path to this final state. The sum of the branching ratio for the two hydroxyl formation channels from HCOOD, Eqs. (6) and (7), is $77.0\% \pm 2.6\%$, in good agreement with the HCOOH branching ratio of $77.1\% \pm 2.4\%$ for hydroxyl formation, which necessarily contains all hydroxyl formation channels. Simple cleavage of the hydroxyl group from the remaining portion of the molecule is ~15 times more likely than OH^+ formation involving the carboxyl hydrogen [Eq. (7)], indicating a propensity for the hydroxyl group to remain intact. Still, bond rearrangement in the hydroxyl formation processes associating an oxygen and the carboxyl hydrogen [Eq. (7)] occurs about 6.5% of the time when a hydroxyl ion is formed in two-body dissociation. This is the third-largest two-body channel observed in the HCOOD experiment. Furthermore, the isotopic purity of the commercial HCOOD sample is >98.7%, so in the worst case the measured level of the $OH^+ + DCO^+$ channel is 5 times the maximum contribution that could be expected from contaminant DCOOH molecules.

The simple cleavage routes to hydroxyl formation [Eqs. (1) and (6)] produce very similar KERs, as shown in Fig. 1. The peak of the KER distribution near 6.2 eV is somewhat higher than the 5.5-eV peak in the previous experiment of Wang *et al.* [46]. In those experiments, the 100-fs pulse duration was kept constant while the intensity was changed between 9.0×10^{13} and 2.4×10^{14} W/cm^2 [46,47]. Since our peak intensity is approximately an order of magnitude higher, it is possible that some population of excited dication states occurs. Unfortunately, as far as we are aware, the only calculated dication

TABLE I. Branching ratios for two-body dissociation channels following double ionization of HCOOH and HCOOD. The equation numbers are listed to the right of the dissociation channel.

Process	HCOOH channel	HCOOH branching ratio (%)	HCOOD channel	HCOOD branching ratio (%)
Hydroxyl formation	$OH^+ + HCO^+$ (1)	77.1 ± 2.4		
			$OD^+ + HCO^+$ (6)	72.3 ± 2.5
			$OH^+ + DCO^+$ (7)	4.69 ± 0.57
Deprotonation	$H^+ + HCO_2^+$ (2)	21.0 ± 2.3		
			$H^+ + DCO_2^+$ (8)	20.1 ± 2.2
			$D^+ + HCO_2^+$ (9)	0.85 ± 0.11
Deoxygenation	$O^+ + H_2CO^+$ (3)	1.12 ± 0.14	$O^+ + HDCO^+$ (10)	1.34 ± 0.17
Water formation	$H_2O^+ + CO^+$ (4)	0.644 ± 0.083	$HDO^+ + CO^+$ (11)	0.632 ± 0.080
Hydrogen formation	$H_2^+ + CO_2^+$ (5)	0.124 ± 0.016	$HD^+ + CO_2^+$ (12)	0.096 ± 0.013

potentials available [47] examine only a specific reaction coordinate originating from the triplet ground state of HCOOH and leading to a different dissociation limit. An estimation of the KER distributions would need calculations of the energies in the Franck-Condon region relative to the dissociation limits for the states involved. We note, however, that the increase in intensity from 9.0×10^{13} to 2.4×10^{14} W/cm^2 did not modify the $OH^+ + HCO^+$ KER distribution in the experiments of Wang *et al.* [46]. Furthermore, while the peak intensity in our experiment was 2×10^{15} W/cm^2, the higher-intensity region of the focal volume is probably the source of the three- and four-body fragmentation in our data. The region of the focal volume producing the two-body double ionization could be at an intensity roughly similar to the conditions reported by Wang *et al.* [46,47]. Thus, a plausible explanation for the higher KER in the present experiment is that the shorter 25-fs pulse duration does not allow the C-OH bond to stretch as far in the field prior to ionization, as has been seen in other molecules [56–58].

As shown in Fig. 1, the bond-rearrangement $OH^+ + DCO^+$ channel has a lower KER than the more commonly occurring $OD^+ + HCO^+$ dissociation [Eq. (6)]. Closer inspection of the KER distribution for the $OH^+ + DCO^+$ channel [Eq. (7)] shows that it is likely that there are multiple contributions to this channel. The sum of two Gaussian-shaped curves fits the measured data reasonably well. The peaks of the two curves are at 4.4 and 5.6 eV. The separation suggests that hydroxyl-forming bond rearrangement connecting an oxygen to the carboxyl hydrogen might occur via two different reaction processes. In fact, there are at least two possible routes that could contribute to a $OH^+ + DCO^+$ final state [Eq. (7)]. In one scenario, the carboxyl hydrogen migrates to form an OH^+ ion with the oxygen atom that was initially double bonded to the carbon atom. In the other scenario, the hydrogen atoms exchange sites, or scramble [17], prior to cleavage of the hydroxyl group. Note that our data do not differentiate between the propagation of nuclear wave packets on multiple potential-energy surfaces and the bifurcation of a wave packet on a single potential-energy surface.

B. Deprotonation

When deuterium tagging is used to determine which proton is removed in the $HCOOH^{2+} \rightarrow H^+ + HCO_2^+$ deprotonation process [Eq. (2)], we find that the carboxyl hydrogen is much more likely ($\sim$30:1) to be separated than the hydroxyl hydrogen. The sum of the branching ratio for the two deprotonation channels from HCOOD is $20.1\% \pm 2.2\%$, in agreement with the branching ratio measured for deprotonation of HCOOH, $21.0\% \pm 2.3\%$. The deprotonations of the carboxyl proton in both isotopologues [Eqs. (2) and (8)] have nearly identical KERs peaked around 5.4 eV, while deprotonation of the hydroxyl deuteron [Eq. (9)] occurs with a KER peaked 0.8 eV lower, as illustrated in Fig. 3.
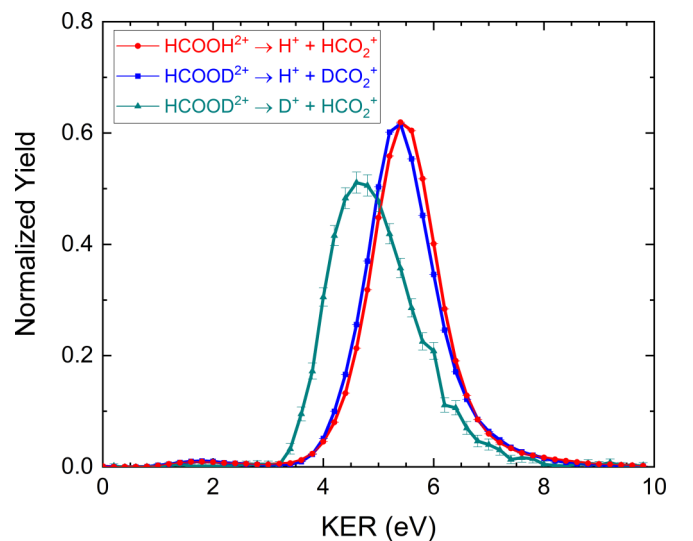

FIG. 3. Normalized yield as a function of KER for deprotonation processes leading to $H^+ + HCO_2^+$ [Eq. (2); red circles], $H^+ + DCO_2^+$ [Eq. (8); blue squares], and $D^+ + HCO_2^+$ [Eq. (9); green triangles]. The normalization sets the integral of the KER distribution to 1 for each channel.

The results from the deprotonation and hydroxyl formation channels explored with deuterium tagging indicate that the OH^+ group is most likely to remain intact following double ionization. Specifically, either the formation of OH^+ with the carboxyl hydrogen [Eq. (7)] or the dissociation of the hydroxyl proton from the rest of the molecular ion is relatively small compared to a process that leaves the original OH group intact. In addition, the KERs of dissociation channels that do not involve an intact OH^+ [Eqs. (6) and (9)] are markedly different than those of the analogous channels containing the intact OH^+.

C. Water formation

Formation of water ions from the formic-acid dication, i.e., $HCOOH^{2+} \rightarrow H_2O^+ + CO^+$ [Eq. (4)], involves multiple bond cleavages and subsequent bond formation. This channel is approximately 5–6 times more likely to occur than bond rearrangement leading to H_2^+ formation. For both of these reasons, $HCOOH^{2+} \rightarrow H_2O^+ + CO^+$ [Eq. (4)] was examined previously from both experimental and theoretical perspectives [47]. In that previous work, Wang *et al.* suggested a two-step process proceeding from the triplet state of the dication. First, the hydrogen atom migrates from the carboxyl site to the hydroxyl site and overcomes the 2.29 eV of the transition state. Second, dissociation to $H_2O^+ + CO^+$ occurs following some evolution to a second transition state. They predicted a KER of 4.96 eV for this process, in good agreement with their experimental KER distribution that was peaked at 4.8 eV [47]. Analogous hydrogen migrations in other dications have been linked to similar processes in small polyatomic molecules exposed to intense laser pulses [5,6,30,31,35,36,39].

As indicated in Table I, the branching ratio for $HDO^+ + CO^+$ [Eq. (11)] is very similar to the branching ratio for $H_2O^+ + CO^+$ [Eq. (4)], suggesting no isotopic dependence. We compare the measured KER distributions of $HCOOH^{2+} \rightarrow H_2O^+ + CO^+$ [Eq. (4)] and $HCOOD^{2+} \rightarrow HDO^+ + CO^+$ [Eq. (11)] in Fig. 4(a). While the two KER distributions are very similar, the peak of the distributions near 5.6 eV is higher, by about 0.8 eV, than what was observed by Wang *et al.* [47]. The trend toward higher KER as a function of intensity is consistent with the increase in the location of the most probable KER value in their data as the intensity increases [47].

D. Hydrogen formation

Hydrogen migration leading to $HCOOH^{2+} \rightarrow H_2^+ + CO_2^+$ [Eq. (5)] formation is the smallest of the two-body breakup channels following double ionization. Within the statistics of our measurement, the branching ratios for $H_2^+ + CO_2^+$ [Eq. (5)] and $HD^+ + CO_2^+$ [Eq. (12)] are the same, again indicating a lack of any significant isotopic effect. A possible explanation for the relative branching ratios of H_2^+ and H_2O^+ is a sequential process which begins with the carboxyl hydrogen migrating to the hydroxyl side of the molecule. At that point dissociation to H_2O^+ may occur, or in a less likely scenario, the carboxyl hydrogen captures only the proton from the hydroxyl group. The observation that the
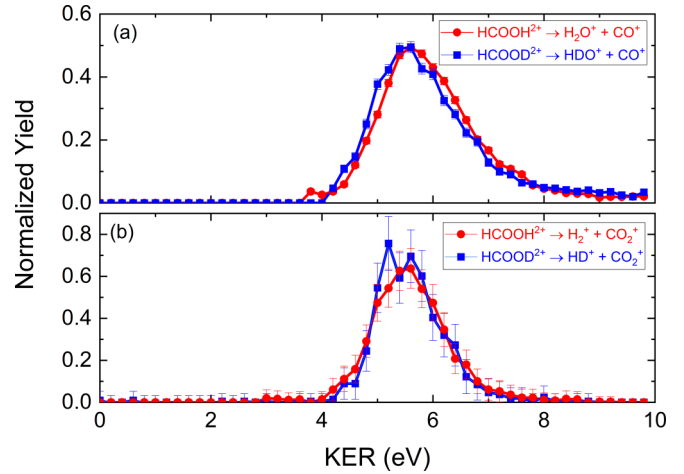

FIG. 4. Normalized yield as a function of KER for two-body breakup channels that involve bond rearrangement. (a) Water formation channels $H_2O^+ + CO^+$ [red circles; Eq. (4)] and $HDO^+ + CO^+$ [blue squares; Eq. (11)]. (b) Hydrogen formation channels $H_2^+ + CO_2^+$ [red circles; Eq. (5)] and $HD^+ + CO_2^+$ [blue squares; Eq. (12)]. As in the other figures, the normalization sets the integral of each KER distribution to 1.

formation of H_2^+ (HD^+) is less likely than the formation of H_2O^+ (HDO^+) is consistent with the idea, discussed above, that the hydroxyl ion is more likely to remain intact than the hydroxyl hydrogen atom is to move independently. In addition, we observe that the KER distributions for both hydrogen formation channels [Eqs. (5) and (12)] are similar, as shown in Fig. 4(b), further supporting the idea that both of the bond-rearrangement channels are initiated by the migration of the carboxyl hydrogen.

E. Deoxygenation

The $HCOOH^{2+} \rightarrow O^+ + H_2CO^+$ deoxygenation process [Eq. (3)] is interesting since there are two scenarios that could lead to these final products. In one scenario, the double bond between the carbon and lone oxygen is broken, and dissociation of the oxygen follows. The other scenario involves more complex dynamics beginning with the hydroxyl hydrogen migrating to the carboxyl site and a subsequent dissociation of the C-O single bond. Wang *et al.* [46] observed this deoxygenation channel and concluded that the dissociation of the double bond was the more likely pathway [47].

In contrast to the single peak KER distribution centered at ~4 eV with a width of about 1.8 eV reported in Ref. [47], the KER distributions we measured have a more complex structure. Figure 5 shows the KER distributions for both the $O^+ + H_2CO^+$ [Eq. (3)] and $O^+ + HDCO^+$ [Eq. (10)] dissociation channels along with corresponding two-Gaussian fits of each channel. The two-Gaussian fit models the data well in both cases. The peaks of the lower-energy components in our fits are at 4.0 eV for $O^+ + HDCO^+$ [Eq. (10)] and 4.1 eV for $O^+ + H_2CO^+$ [Eq. (3)]. Both of these peaks are similar to the peak of the KER distribution observed for this channel with 100-fs, 0.9×10^{14} and 2.4×10^{14} W/cm^2 pulses by Wang *et al.* [47]. The higher KER peak, centered near 5.1 eV in the deoxygenation channels of both isotopologues,
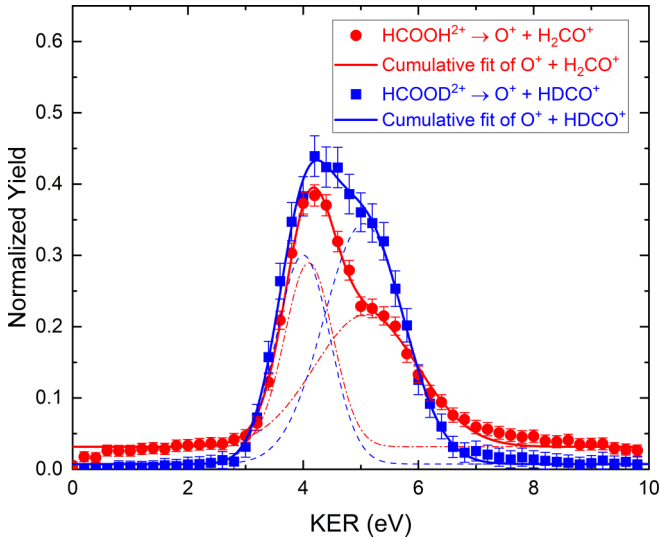
FIG. 5. Normalized yield of the deoxygenation channels as a function of KER for the $O^+ + H_2CO^+$ (red circles) and $O^+ + HDCO^+$ (blue squares) dissociation channels. Both KER distributions are fit with the sum of two Gaussian curves, where the individual Gaussian curves are shown by the red dash-dotted and blue dashed lines for $O^+ + H_2CO^+$ and $O^+ + HDCO^+$, respectively. The centers of the component Gaussian curves are found to be at 4.1 and 5.1 eV for $O^+ + H_2CO^+$ and at 4.0 and 5.1 eV for $O^+ + HDCO^+$. The thick solid lines are the sum of the two Gaussian curves.

however, is an additional feature that occurs in our measurements due to the increased intensity and/or the shorter pulse duration. Since the migration of the hydroxyl hydrogen, the initial step in the second pathway described above, is essentially the inverse of the hydrogen migration that is thought to begin the process leading to the observed H_2O^+ formation [Eqs. (4) and (11)], it is possible that this second pathway is also active. The peak and width of the KER distributions for water formation [Eqs. (4) and (11)], shown in Fig. 4(a), are similar to the higher-energy component of the $O^+ + H_2CO^+$ KER distribution shown in Fig. 5. As discussed in the Appendix, the angular distributions of the water formation and deoxygenation channels also show some similarities. Interestingly, the higher-energy component seems more prevalent for the $O^+ + HDCO^+$ channel [Eq. (10)] than for $O^+ + H_2CO^+$ [Eq. (3)]. This speculation about the origin of the higher-energy KER component in the deoxygenation channels may serve as a guide for future theoretical investigations.

IV. SUMMARY

Using a COLTRIMS coincidence momentum imaging technique, we have measured the branching ratio and three-dimensional momentum distributions of two-body breakup channels resulting from dissociative double ionization of formic acid by ultrashort intense laser pulses. By using deuterium tagging to differentiate the hydroxyl and carboxyl hydrogen atoms, we observed a clear preference for the OH (OD) structure to remain intact. When the O-H hydroxyl structure is separated, the KER is reduced compared to channels with analogous final products that keep the hydroxyl

group together. While deuterium tagging was useful for gaining additional insight into the roles of the hydroxyl and carboxyl hydrogen atoms, we did not observe statistically significant isotopic differences between analogous HCOOH and HCOOD dissociation channels under our experimental conditions. The hydroxyl formation, $HCOOD^{2+} \rightarrow OH^+ + DCO^+$, and deoxygenation, $HCOOH^{2+} \rightarrow O^+ + H_2CO^+$, channels showed indications that they are formed by more than one pathway, making them interesting candidates for future study. We hope that this collection of results will motivate theoretical investigations exploring the bond rearrangement and fragmentation dynamics.

APPENDIX: ANGULAR DISTRIBUTIONS

In addition to the KER data presented above, we obtain the angular distribution of the fragment ions relative to the polarization direction from the COLTRIMS measurement. Angular distributions can provide stringent tests for theoretical studies of fragmentation dynamics (e.g., Refs. [59–61]), so we include these experimental results here.

Angular distributions from photoionization have traditionally been characterized using the anisotropy parameters β_n [62,63], where

$$W(\cos\theta) = \frac{W_0}{4\pi}\left(1 + \sum_{n>0}\beta_n P_n(\cos\theta)\right) \quad (A1)$$

is the angular distribution, $P_n(\cos\theta)$ are the Legendre polynomials in $\cos\theta$, and θ is the angle between the direction of the less massive fragment in the ion pair and the laser polarization direction. Due to the symmetry in the dissociation processes relative to the linear polarization of the laser, only the even β_n terms contribute to the sum in Eq. (A1). The results of these fits are summarized in Table II and shown in Figs. 6–9. The W_0 term is a constant, so a fit with all $\beta_n = 0$ represents an isotropic angular distribution. The need for higher-order coefficients $\beta_2, \beta_4, \dots, \beta_n$ as fit parameters indicates that the distribution is more strongly peaked along the polarization

TABLE II. The anisotropy parameters β_n [see Eq. (A1)] obtained by fitting the probability of dissociative double ionization leading to two-body breakup of HCOOH or HCOOD as a function of $\cos\theta$. The fitting function always included up to β_8, but the table shows only the statistically significant β_n parameters. The equation numbers are listed to the right of each dissociation channel. For consistency, the β_n fits were obtained using the full KER range of each channel.

Dissociation channel	β_2	β_4
$OH^+ + HCO^+$ (1)	0.519 ± 0.019	0.0801 ± 0.025
$OD^+ + HCO^+$ (6)	0.570 ± 0.015	0.0585 ± 0.021
$OH^+ + DCO^+$ (7)	1.05 ± 0.028	0.426 ± 0.037
$H^+ + HCO_2^+$ (2)	0.450 ± 0.016	0.0773 ± 0.021
$H^+ + DCO_2^+$ (8)	0.371 ± 0.009	0.0546 ± 0.012
$D^+ + HCO_2^+$ (9)	0.195 ± 0.044	
$O^+ + H_2CO^+$ (3)	0.863 ± 0.024	0.319 ± 0.033
$O^+ + HDCO^+$ (10)	0.987 ± 0.046	0.340 ± 0.061
$H_2O^+ + CO^+$ (4)	0.883 ± 0.052	0.301 ± 0.070
$HDO^+ + CO^+$ (11)	0.962 ± 0.058	0.402 ± 0.078
$H_2^+ + CO_2^+$ (5)	0.345 ± 0.055	
$HD^+ + CO_2^+$ (12)	0.45 ± 0.11	

direction and thus needs to be characterized with higher-order Legendre polynomials.

In principle, assuming that rotation during and after dissociation can be neglected, i.e., the axial-recoil approximation is valid, the anisotropy parameters can be used to deduce information about the dication state(s) contributing to a particular dissociation channel [64]. This type of analysis, however, is most effective when combined with other information, such as KER, photoelectron spectra, and potential-energy surfaces. While that sort of effort is beyond the scope of this article, the angular distributions reported here can illuminate possibilities for more detailed future work.

In Fig. 6 we show the angular distribution for hydroxyl formation [Eqs. (1), (6), and (7)] as a function of $\cos\theta$. It is readily apparent that the hydroxyl formation leads to fragments that preferentially lie along the laser polarization direction. The similarity of the simple cleavage channels [Eqs. (1) and (6)] extends to their angular distributions, both shown in Fig. 6(a).

Figure 6(b), however, reveals that formation of a hydroxyl ion via a bond-rearrangement process [Eq. (7)] results in OH^+ fragments that are more likely to be emitted along the laser polarization than the simple cleavage channels [Eqs. (1) and (6)]. If the hydrogen migrates to the lone oxygen, the subsequent weakening of the C-O bond could cause relatively rapid dissociation into $OH^+ + DCO^+$. In this case, the emission of $OH^+ + DCO^+$ along the laser polarization is not surprising. On the other hand, if a H/D exchange is followed by a cleavage of the hydroxyl group, the H/D exchange process would presumably take more time than a simple cleavage of the C-O bond leading to OD^+ formation from the HCOOD target [Eq. (6)]. In this H/D exchange scenario, one would expect the bond-rearrangement photofragments [Eq. (7)] to be less tightly centered around the laser polarization than the photofragments from simple cleavage [Eq. (6)], the opposite of our results. The observed angular distributions might there-
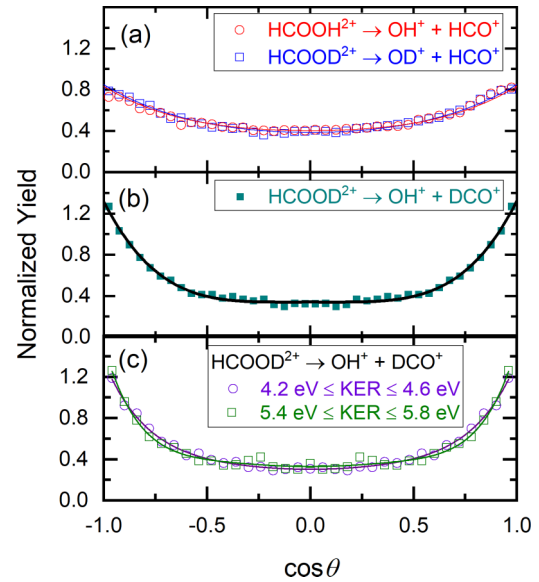

FIG. 6. The normalized yield of the hydroxyl formation channels as a function of $\cos\theta$, where θ is the angle between the lighter fragment ion and the laser polarization direction. Each channel is normalized so the integral of the angular distribution is 1. The statistical uncertainty of these channels is less than the symbol size. (a) OH^+ (red circles) and OD^+ (blue squares) fragments from $HCOOH^{2+} \rightarrow OH^+ + HCO^+$ and $HCOOD^{2+} \rightarrow OD^+ + HCO^+$, respectively. (b) The same plot for OH^+ fragments from $HCOOD^{2+} \rightarrow OH^+ + DCO^+$. These data are mirrored about $\cos\theta = 0$ as described in Sec. II. (c) The $HCOOD^{2+} \rightarrow OH^+ + DCO^+$ angular distributions for KER ranges of 4.4 ± 0.2 eV (violet circles) and 5.6 ± 0.2 eV (olive squares). In each plot, the solid lines represent the fit of Eq. (A1) to the data. The fitting parameters are listed in Table II.

fore suggest hydrogen migration to the lone oxygen is more likely than the H/D exchange. Alternatively, the two processes might not occur on the same potential-energy surface, and thus, the angular distributions of the final states could primarily depend on the ionization step.

Moreover, the KER analysis described in Sec. III A suggested that there are two components in the KER distribution for hydroxyl formation [Eq. (7)], further suggesting that more than one pathway may be active. In Fig. 6(c), we separate the $HCOOD^{2+} \rightarrow OH^+ + DCO^+$ angular distributions into two regions for KER values within ± 0.2 eV of both a KER of 4.4 eV and a KER of 5.6 eV. These KER values are the maxima of the two-component KER fit, as denoted by the lines in Fig. 2(b). The angular distributions obtained from these two KER windows are very similar.

Figures 7(a) and 7(b) show the angular distributions of all three deprotonation channels [Eqs. (2), (8), and (9)]. The angular distributions of the carboxyl deprotonation channels are similar to each other. The angular distribution of the D^+ channel [Eq. (9)], displayed in Fig. 7(a), is less aligned along the laser polarization than the angular distributions of carboxyl deprotonation channel [Eq. (8)] and the combined deprotonation channel [Eq. (2)], shown in Fig. 7(b). These angular distributions can provide guidance to future theoretical models.
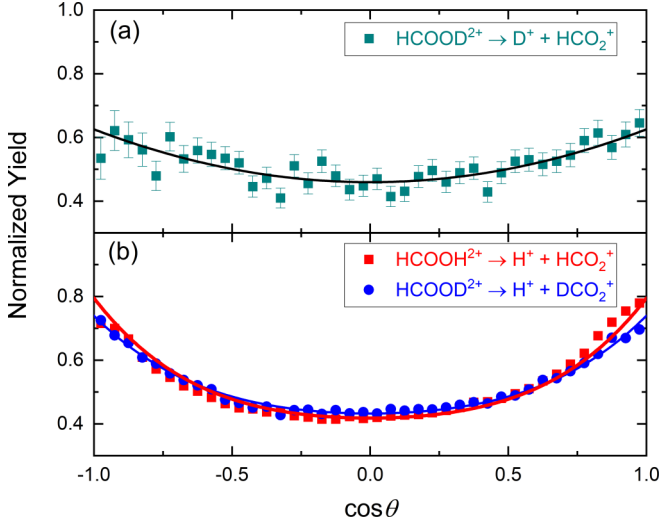
FIG. 7. (a) The normalized yield as a function of $\cos\theta$ for $D^+ + HCO_2^+$, the removal of the hydroxyl proton. When no error bars are shown, the statistical error is less than the symbol size. (b) The normalized yield as a function of $\cos\theta$ for the $H^+ + HCO_2^+$ (red squares) and $H^+ + DCO_2^+$ (blue circles) deprotonation channels involving the removal of the carboxyl proton. The solid lines in (a) and (b) represent fits of Eq. (A1) to the data. The associated anisotropy parameters are listed in Table II.

As shown in Figs. 8(a) and 8(b), the angular distributions of the water formation channels [Eqs. (4) and (11)] do not show any significant isotopic effects. The fitted anisotropy parameters, listed in Table II, quantify this statement. Similarly,
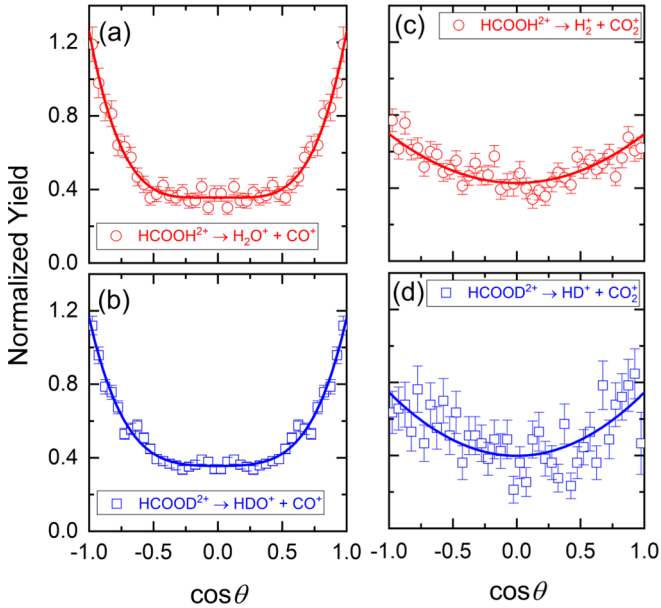

FIG. 8. Left: Normalized yields of water formation as a function of $\cos\theta$ for (a) H_2O^+ [Eq. (4)] and (b) HDO^+ [Eq. (11)]. Right: Normalized yields for (c) H_2^+ [Eq. (5)] and (d) HD^+ formation [Eq. (12)] as a function of $\cos\theta$. In each panel, the solid line shows the fit of the data to Eq. (A1), with the fitting parameters listed in Table II. The water formation angular distributions are obtained by reflecting the data about $\cos\theta = 0$.
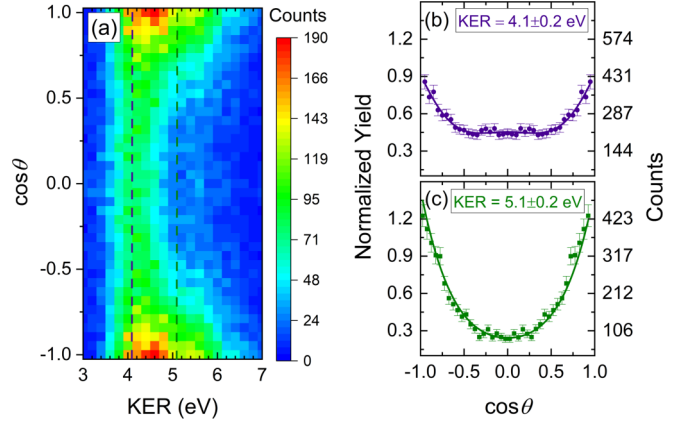

FIG. 9. (a) The number of $HCOOH^{2+} \rightarrow O^+ + H_2CO^+$ deoxygenation events [Eq. (3)] as a function of KER and $\cos\theta$. The dashed vertical lines indicate the center of the regions used to construct the angular distributions shown in the (b) and (c). (b) Normalized yield of deoxygenation [Eq. (3)] as a function of $\cos\theta$ for KER within the range 4.1 ± 0.2 eV. (c) The same plot, except for the higher 5.1 ± 0.2 eV KER range. All of these angular distributions are obtained by reflecting the data about $\cos\theta = 0$. In each plot, the solid line represents the fit of the data to Eq. (A1).

Figs. 8(c) and 8(d) show that the angular distribution of the H_2^+ fragments is essentially similar to the angular distribution of the HD^+ fragments under these experimental conditions.

Unlike hydroxyl formation via $HCOOD^{2+} \rightarrow OH^+ + DCO^+$ [Eq. (7)], for which the angular distributions from the different components of the KER distribution are very similar (Fig. 6), the different KER components of the deoxygenation channels show different angular behavior. Figure 9(a) presents the distribution of $HCOOH^{2+} \rightarrow O^+ + H_2CO^+$ events [Eq. (3)] as a function of KER and $\cos\theta$. From this visualization, it is clear that the number of events that are recorded around $\cos\theta = 0$ falls off as the KER increases.

The propensity of the higher-KER O^+ fragments to be aligned with the polarization axis is quantified using projections, plotted in Figs. 9(b) and 9(c), from a ± 0.2-eV window around the maxima of the two-component KER fit shown in Fig. 5. To quantify the difference in angular distributions from the two regions of the $O^+ + H_2CO^+$ ($O^+ + HDCO^+$) KER distribution, the β_n parameters are obtained using data

TABLE III. The anisotropy parameters β_n [see Eq. (A1)] obtained by fitting the probability of $O^+ + H_2CO^+$ [Eq. (3)] or $O^+ + HDCO^+$ [Eq. (10)] double-ionization events within the indicated KER window as a function of $\cos\theta$. The fitting function always included up to β_8, but only the statistically significant β_n parameters are shown.

Parent molecule	KER window (eV)	β_2	β_4
HCOOH	4.1 ± 0.2	0.521 ± 0.026	0.213 ± 0.028
HCOOH	5.1 ± 0.2	1.32 ± 0.07	0.248 ± 0.047
HCOOD	4.0 ± 0.2	0.554 ± 0.060	0.317 ± 0.056
HCOOD	5.1 ± 0.2	1.28 ± 0.08	0.039 ± 0.055

restricted to the KER windows shown in Fig. 9 and are reported in Table III.

The parameters of the angular fits, shown in Table III, verify that there is a significant difference between the angular distribution of the O^+ fragments in these two KER regions. The β_2 parameters from the higher-KER deoxygenation channels seem to most resemble water formation and the bond-rearrangement route to hydroxyl formation [Eq. (7)]. In addition, while the two components of the O^+ KER distribution are more clearly visible from the HCOOH par-

ent molecule, the KER-window-specific angular distributions arising from the HCOOH and HCOOD isotopologues are similar.

A general remark about the hydrogen migration and bond-rearrangement channels in formic acid is that they are more strongly peaked along $\cos\theta = \pm 1$ than some similar processes in other small molecules, such as $H_3{}^+$ formation from methanol [35,39] or vinylidenelike dissociation of acetylene ($C_2H_2{}^{2+} \rightarrow CH_2{}^+ + C^+$) [10,65] following double ionization.

[1] D. Townsend, S. A. Lahankar, S. K. Lee, S. D. Chambreau, A. G. Suits, X. Zhang, J. Rheinecker, L. B. Harding, and J. M. Bowman, Science **306**, 1158 (2004).

[2] N. Herath and A. G. Suits, J. Phys. Chem. Lett. **2**, 642 (2011).

[3] J. M. Bowman and A. G. Suits, Phys. Today **64**(11), 33 (2011).

[4] J. M. Bowman, Mol. Phys. **112**, 2516 (2014).

[5] N. Ekanayake, M. Nairat, B. Kaderiya, P. Feizollah, B. Jochim, T. Severt, B. Berry, K. Raju P., K. D. Carnes, S. Pathak, D. Rolles, A. Rudenko, I. Ben-Itzhak, C. A. Mancuso, B. S. Fales, J. E. Jackson, B. G. Levine, and M. Dantus, Sci. Rep. **7**, 4703 (2017).

[6] N. Ekanayake, T. Severt, M. Nairat, N. P. Weingartz, B. M. Farris, B. Kaderiya, P. Feizollah, B. Jochim, F. Ziaee, K. Borne, K. Raju P., K. D. Carnes, D. Rolles, A. Rudenko, B. G. Levine, J. E. Jackson, I. Ben-Itzhak, and M. Dantus, Nat. Commun. **9**, 5186 (2018).

[7] W. Fuß, W. Schmid, and S. Trushin, Chem. Phys. **316**, 225 (2005).

[8] T. Okino, Y. Furukawa, P. Liu, T. Ichikawa, R. Itakura, K. Hoshina, K. Yamanouchi, and H. Nakano, Chem. Phys. Lett. **419**, 223 (2006).

[9] T. Okino, Y. Furukawa, P. Liu, T. Ichikawa, R. Itakura, K. Hoshina, K. Yamanouchi, and H. Nakano, Chem. Phys. Lett. **423**, 220 (2006).

[10] A. Hishikawa, A. Matsuda, M. Fushitani, and E. J. Takahashi, Phys. Rev. Lett. **99**, 258302 (2007).

[11] A. M. Mebel and A. D. Bandrauk, J. Chem. Phys. **129**, 224311 (2008).

[12] H. Xu, T. Okino, and K. Yamanouchi, Chem. Phys. Lett. **469**, 255 (2009).

[13] H. Xu, T. Okino, and K. Yamanouchi, J. Chem. Phys. **131**, 151102 (2009).

[14] K. Hoshina, H. Kawamura, M. Tsuge, M. Tamiya, and M. Ishiguro, J. Chem. Phys. **134**, 064324 (2011).

[15] T. K. Allison, H. Tao, W. J. Glover, T. W. Wright, A. M. Stooke, C. Khurmi, J. van Tilborg, Y. Liu, R. W. Falcone, T. J. Martínez, and A. Belkacem, J. Chem. Phys. **136**, 124317 (2012).

[16] T. Okino, A. Watanabe, H. Xu, and K. Yamanouchi, Phys. Chem. Chem. Phys. **14**, 4230 (2012).

[17] R. Kanya, T. Kudou, N. Schirmel, S. Miura, K.-M. Weitzel, K. Hoshina, and K. Yamanouchi, J. Chem. Phys. **136**, 204309 (2012).

[18] L. Belshaw, F. Calegari, M. J. Duffy, A. Trabattoni, L. Poletto, M. Nisoli, and J. B. Greenwood, J. Phys. Chem. Lett. **3**, 3751 (2012).

[19] S. Maclot, D. G. Piekarski, A. Domaracka, A. Méry, V. Vizcaino, L. Adoui, F. Martín, M. Alcamí, B. A. Huber, P. Rousseau, and S. Díaz-Tendero, J. Phys. Chem. Lett. **4**, 3903 (2013).

[20] N. Kotsina, S. Kaziannis, and C. Kosmidis, Chem. Phys. Lett. **604**, 27 (2014).

[21] H. Ibrahim, B. Wales, S. Beaulieu, B. E. Schmidt, N. Thiré, E. P. Fowe, É. Bisson, C. T. Hebeisen, V. Wanie, M. Giguére, J.-C. Kieffer, M. Spanner, A. D. Bandrauk, J. Sanderson, M. S. Schuurman, and F. Légaré, Nat. Commun. **5**, 4422 (2014).

[22] H. Wu, S. Zhang, J. Zhang, Y. Yang, L. Deng, T. Jia, Z. Wang, and Z. Sun, J. Phys. Chem. A **119**, 2052 (2015).

[23] P. Ma, C. Wang, X. Li, X. Yu, X. Tian, W. Hu, J. Yu, S. Luo, and D. Ding, J. Chem. Phys. **146**, 244305 (2017).

[24] N. G. Kling, S. Díaz-Tendero, R. Obaid, M. R. Disla, H. Xiong, M. Sundberg, S. D. Khosravi, M. Davino, P. Drach, A. M. Carroll, T. Osipov, F. Martín, and N. Berrah, Nat. Commun. **10**, 2813 (2019).

[25] M. Kübel, R. Siemering, C. Burger, N. G. Kling, H. Li, A. S. Alnaser, B. Bergues, S. Zherebtsov, A. M. Azzeer, I. Ben-Itzhak, R. Moshammer, R. de Vivie-Riedle, and M. F. Kling, Phys. Rev. Lett. **116**, 193001 (2016).

[26] Y. Furukawa, K. Hoshina, K. Yamanouchi, and H. Nakano, Chem. Phys. Lett. **414**, 117 (2005).

[27] T. Okino, Y. Furukawa, P. Liu, T. Ichikawa, R. Itakura, K. Hoshina, K. Yamanouchi, and H. Nakano, J. Phys. B **39**, S515 (2006).

[28] K. Hoshina, Y. Furukawa, T. Okino, and K. Yamanouchi, J. Chem. Phys. **129**, 104302 (2008).

[29] S. Kaziannis, I. Liontos, G. Karras, C. Corsi, M. Bellini, and C. Kosmidis, J. Chem. Phys. **131**, 144308 (2009).

[30] P. M. Kraus, M. C. Schwarzer, N. Schirmel, G. Urbasch, G. Frenking, and K.-M. Weitzel, J. Chem. Phys. **134**, 114302 (2011).

[31] N. Schirmel, N. Reusch, P. Horsch, and K.-M. Weitzel, Faraday Discuss. **163**, 461 (2013).

[32] S. Sun, Y. Yang, J. Zhang, H. Wu, Y. Chen, S. Zhang, T. Jia, Z. Wang, and Z. Sun, Chem. Phys. Lett. **581**, 16 (2013).

[33] N. Kotsina, S. Kaziannis, and C. Kosmidis, Int. J. Mass Spectrom. **380**, 34 (2015).

[34] N. Ekanayake, M. Nairat, N. P. Weingartz, M. J. Michie, B. G. Levine, and M. Dantus, J. Chem. Phys. **149**, 244310 (2018).

[35] T. Ando, A. Shimamoto, S. Miura, A. Iwasaki, K. Nakai, and K. Yamanouchi, Commun. Chem. **1**, 7 (2018).

[36] Y. Boran, G. L. Gutsev, A. A. Kolomenskii, F. Zhu, A. Schuessler, and J. Strohaber, J. Phys. B **51**, 035003 (2018).

[37] T. Ando, A. Iwasaki, and K. Yamanouchi, Mol. Phys. **117**, 1732 (2019).

[38] S. Zhao, B. Jochim, P. Feizollah, J. Rajput, F. Ziaee, K. Raju P., B. Kaderiya, K. Borne, Y. Malakar, B. Berry, J. Harrington, D. Rolles, A. Rudenko, K. D. Carnes, E. Wells, I. Ben-Itzhak, and T. Severt, Phys. Rev. A **99**, 053412 (2019).

[39] N. Iwamoto, C. J. Schwartz, B. Jochim, K. Raju P., P. Feizollah, J. L. Napierala, T. Severt, S. N. Tegegn, A. Solomon, S. Zhao, H. Lam, T. N. Wangjam, V. Kumarappan, K. D. Carnes, I. Ben-Itzhak, and E. Wells, J. Chem. Phys. **152**, 054302 (2020).

[40] T. Townsend, C. J. Schwartz, B. Jochim, K. Raju P., T. Severt, N. Iwamoto, J. L. Napierala, P. Feizollah, S. N. Tegegn, A. Solomon, S. Zhao, K. D. Carnes, I. Ben-Itzhak, and E. Wells, Front. Phys. **9**, 364 (2021).

[41] M. Pettersson, E. M. S. Maçôas, L. Khriachtchev, R. Fausto, and M. Räsänen, J. Am. Chem. Soc. **125**, 4058 (2003).

[42] N. S. Shuman, M. Johnson, W. R. Stevens, M. E. Harding, J. F. Stanton, and T. Baer, J. Phys. Chem. A **114**, 10016 (2010).

[43] T. Ng and S. Bell, J. Mol. Spectrosc. **50**, 166 (1974).

[44] L. M. Beaty-Travis, D. C. Moule, E. C. Lim, and R. H. Judge, J. Chem. Phys. **117**, 4831 (2002).

[45] K. Fehre, S. Eckart, M. Kunitski, M. Pitzer, S. Zeller, C. Janke, D. Trabert, J. Rist, M. Weller, A. Hartung, L. P. H. Schmidt, T. Jahnke, R. Berger, R. Dörner, and M. S. Schöffler, Sci. Adv. **5**, eaau7923 (2019).

[46] C. Wang, D. Ding, M. Okunishi, Z.-G. Wang, X.-J. Liu, G. Prümper, and K. Ueda, Chem. Phys. Lett. **496**, 32 (2010).

[47] C. Wang, B. Wang, M. Okunishi, W. Roeterdink, D. Ding, R. Zhu, G. Prümper, K. Shimada, and K. Ueda, Chem. Phys. **430**, 40 (2014).

[48] X. Ren, A. M. Summers, K. Raju P., A. Vajdi, V. Makhija, C. W. Fehrenbach, N. G. Kling, K. J. Betsch, Z. Wang, M. F. Kling, K. D. Carnes, I. Ben-Itzhak, C. Trallero-Herrero, and V. Kumarappan, J. Opt. **19**, 124017 (2017).

[49] R. Dörner, V. Mergel, O. Jagutzki, L. Spielberger, J. Ullrich, R. Moshammer, and H. Schmidt-Böcking, Phys. Rep. **330**, 95 (2000).

[50] J. Ullrich, R. Moshammer, A. Dorn, R. Dörner, L. P. H. Schmidt, and H. Schmidt-Böcking, Rep. Prog. Phys. **66**, 1463 (2003).

[51] T. Jahnke *et al.*, in *Molecular Beams in Physics and Chemistry* (Springer, Cham, Switzerland, 2021), pp. 375–441.

[52] G. F. Knoll, *Radiation Detection and Measurement* (Wiley, Hoboken, NJ, 2010).

[53] E. Bjarnov and W. H. Hocking, Z. Naturforsch. A **33**, 610 (1978).

[54] K. A. E. Meyer and M. A. Suhm, Chem. Sci. **10**, 6285 (2019).

[55] P. Atkins, J. Depaula, J. Keeler, and J. de Paula, *Atkins' Physical Chemistry* (Oxford University Press, Oxford, 2018).

[56] J. H. Posthumus, A. J. Giles, M. R. Thompson, and K. Codling, J. Phys. B **29**, 5811 (1996).

[57] Q. Liang, C. Wu, Z. Wu, M. Liu, Y. Deng, and Q. Gong, Phys. Rev. A **79**, 045401 (2009).

[58] X. Xie, E. Lötstedt, S. Roither, M. Schöffler, D. Kartashov, K. Midorikawa, A. Baltuška, K. Yamanouchi, and M. Kitzler, Sci. Rep. **5**, 12877 (2015).

[59] A. Hishikawa, S. Liu, A. Iwasaki, and K. Yamanouchi, J. Chem. Phys. **114**, 9856 (2001).

[60] A. M. Sayler, P. Q. Wang, K. D. Carnes, B. D. Esry, and I. Ben-Itzhak, Phys. Rev. A **75**, 063420 (2007).

[61] Z. Li, L. Inhester, C. Liekhus-Schmaltz, B. F. E. Curchod, J. W. Snyder, N. Medvedev, J. Cryan, T. Osipov, S. Pabst, O. Vendrell, P. Bucksbaum, and T. J. Martinez, Nat. Commun. **8**, 453 (2017).

[62] R. N. Zare, Mol. Photochem. **4**, 1 (1972).

[63] L. Giannessi, E. Allaria, K. C. Prince, C. Callegari, G. Sansone, K. Ueda, T. Morishita, C. N. Liu, A. N. Grum-Grzhimailo, E. V. Gryzlova, N. Douguet, and K. Bartschat, Sci. Rep. **8**, 7774 (2018).

[64] M. Kanno, B. Mignolet, F. Remacle, and H. Kono, J. Chem. Phys. **154**, 224304 (2021).

[65] T. Osipov, C. L. Cocke, M. H. Prior, A. Landers, T. Weber, O. Jagutzki, L. Schmidt, H. Schmidt-Böcking, and R. Dörner, Phys. Rev. Lett. **90**, 233002 (2003).